Synthesis of a Highly Programmable Multistable Kresling Origami-Inspired Unit Cell

Richard Rodriguez-Feliciano, K. W. Wang

Department of Mechanical Engineering, University of Michigan, Ann Arbor, MI, USA 48109

Keywords:

Origami-inspired, Reconfigurable structures, Programmable multistability, Mechanical property tailoring, Modularity

Abstract:

Multistable origami structures have been exploited for mechanical property tailoring, deployable robotic arms, wave propagation tuning and others, due to its ability to possess multiple stable states with distinct properties. Traditionally these structures are made by assembling bistable unit cells, which results in a significant increase in the size and weight of the system when larger number of stable states are required. Recently, researchers have uncovered a third stable state in the Kresling origami pattern. Although this is an advancement over the bistable unit cell, there is an unexplored opportunity for more systematically expanding the design space of Kresling unit cells to possess many more stable configurations (>>2) and enhance its programmable multistability. In this research, we seek to develop a methodology for the design of a Kresling origami-inspired unit cell that can be easily programmed to achieve up to 10 stable configurations, with the potential to achieve even more. We exploit the rich kinematics of the Kresling origami-inspired unit cell, that arise from its coupled translational and rotational deployment, and propose the strategic integration of tensile elements to realize multiple stable states. Analytically, we study the unstretched length values (defined to be the precise length between the string "slacked" and "tensioned" configurations) of the strings that yield the distinct number of stable states. We present the potential energy profiles with its corresponding force-displacement plots for the bistable, tristable, quadstable, pentastable and decastable unit cells. Moreover, we show that by simply adjusting the unstretched length of the strings we can program and tune the number of stable states of the unit cell. Tristable and pentastable unit cell prototypes are designed and experimentally tested to validate the proposed methodology. Lastly, a study is performed on the mechanical property tailoring capabilities of two unit cells assembled in series. The results show that the decastable unit cell assembly can achieve up to 55 discrete values of equivalent stiffness, while the bistable one can only achieve 3. For the bistable unit cell assembly to match this number, it will require 54 unit cells in series, which will significantly increase the size and weight of the structural system. These findings show that the modular structure will have more programmable capabilities, while maintaining its size and weight at a minimum, as the number of stable states per unit cell is increased.

Introduction:

Origami, the art of paper folding, creates sophisticated three-dimensional (3D) structures from flat sheets. It has gained the attention of engineers and scientists due to its deployment characteristics and rich mechanical properties (auxetics, stiffness tuning, multistability, etc.) [1–7]. Origami patterns can be divided into rigid (deformation only occurs in creases) and nonrigid (deformation occurs in both the creases and panels) foldable. One of the most common patterns of rigid foldable origami is the Miura-Ori [8,9]. This origami pattern is a flat foldable degree-4 vertex that connects four parallelograms. Many studies on Miura-ori have focused on the kinematics, mechanical behavior and dynamic response of a single degree-4 vertex sheet [10–19] and of two stacked single degree-4 vertex sheets forming tubular or cellular structure [20–28]. On the other hand, one of the most common non-rigid foldable origami patterns is Kresling, named after Biruta Kresling [29]. This origami pattern is a twist buckled multifunctional cylindrical structure [30–32]. Hence, this pattern undergoes a coupled translational and rotational deformation while deploying. A common phenomenon observed in the deployment of a Kresling unit cell is the ability to have two stable configurations (bistability). These features have led researchers to study its many interesting mechanics characteristics, dynamic behaviors, and engineering functionalities [33–47]. Since this pattern undergoes panel deformation when deploying, distinct methodologies have been proposed for its modeling [48–50]. Two well-known approaches consist of modeling the facets and creases with a truss that deforms axially

[48,49], and the other consists of a system that models panel bending with "virtual folds" [50]. These methodologies have accurately predicted and modeled bistability in Kresling.

Realizing more than two stable configurations in Kresling origami has been previously proposed by connecting multiple bistable unit cells in series [51–53]. This comes at the cost of increasing the size and weight of the structure. Having only two stable configurations per unit cell also limits the programmability of the system. Hence, a programmable unit cell capable of achieving even more stable configurations can greatly enhance the ability to accomplish more tasks with fewer components. For example, it can better tune the mechanical properties of a system [54–56], increase the number of deployed states [57–60], better tailor wave propagation in a chain of Kresling origamis [61–64], and create combinatorial mechanical logic systems [65–68]. Recently, researchers have explored achieving three stable configurations in a single Kresling unit cell [69–72]. Tristability has been achieved by creating a conical design of Kresling with creases that pop outward [69,70], by creating a magneto-Kresling truss [71] and by introducing bioinspired nonlinear creases [72]. All of these works exploited modifications of the traditional Kresling design to achieve three stable configurations in a single unit cell. While these tristable Kresling unit cells offer greater programmability, compared to their bistable counterparts, multistable states that are greater than three per unit cell have yet to be discovered. More importantly, there is lack of a rigorous platform that can uncover a broad design space that allows one to systematically design the desired number of stable configurations in a single unit cell.

To advance the state of the art, in this study, we propose a methodology for the design of a Kresling origami-inspired unit cell with programmable multistability that can achieve many more (e.g., ten) stable configurations. Researchers have previously implemented elastic strings (i.e., *tensile elements* that cannot take compression loads) in origami for the purpose of actuation and property tuning [73–79], as well as for transforming a monostable Miura-ori unit cell into a bistable one [79]. Inspired by these efforts, in this study we seek to significantly advance the state of the art and uncover a programmable multistable (>>2)

Kresling origami-inspired unit cell by exploiting the rich kinematics of Kresling's coupled translational and rotational motion and its integration and interaction with tensile elements.

The remainder of this paper is divided as follows. In Section 2 we present the proposed Kresling origami-inspired unit cell. In this section we demonstrate how its kinematics, and the implementation of strings connections uncovers new stable configurations in the unit cell. Section 3 contains the design methodology of the proposed unit cell that can achieve up to ten stable configurations. This section also contains the experimental validation of a unit cell that can achieve three and five stable states. In Section 4, we present a case study that demonstrates the effects of multistable unit cells on the mechanical property tailoring capabilities of a modular structure. Section 5 summarizes the main findings of this work.

Section 2: Kresling Origami-Inspired Unit Cell

In this section we show that by exploiting the rich kinematics of the proposed Kresling origami-inspired unit cell with the strategic integration of tensile elements between its nodes we can achieve many stable configurations (>>2). First, we present a detailed description of the proposed unit cell and show the kinematics for the case of the six-sided polygon. Then, we show that a stable configuration at a specific height value can be realized if we have two strings with opposing changes in length. Lastly, we show that by increasing the number of nodes in the top and bottom polygons we can increase the number of regions where we can achieve a distinct stable configuration.

The deployment of a classical Kresling origami (geometry illustrated in Figure 1a) cannot be modeled by pure folding of its creases; it requires the bending and stretching of its triangular panels. In this work, we propose a Kresling origami-inspired design by replacing the triangular facets with a rigid bar that is allowed to freely rotate at its joints without torsional springs (i.e., we assume that no strain energy storage elements at the creases/joints), as illustrated in Figure 1b. This assumption allows for modeling the height, H, of the unit cell as a function of the rotational angle of the structure, α. For the case of six sided unit cell ($N = 6$), the distance between nodes 1 and 7 can be expressed as:

$$D_{1-7}{}^2 = (x_7 - x_1)^2 + (y_7 - y_1)^2 + (z_7 - z_1)^2, \qquad 2.1$$

where D_{1-7} is the distance between nodes 1 and 7, and the variables x_i, y_i and z_i are the coordinates of each node. From the rigid bar assumption D_{1-7} is equal to the length of the bar, L_b. The height of the structure, H, is the difference between the z-coordinate value of nodes 1 and 7. Thus, 2.1 can be solved for the height of the structure as follows:

$$L_b{}^2 = (x_7 - x_1)^2 + (y_7 - y_1)^2 + H^2, \qquad 2.2$$

$$H = \sqrt{L_b{}^2 - (x_7 - x_1)^2 - (y_7 - y_1)^2}. \qquad 2.3$$

If the bottom polygon remains fixed and the top is rotated as a function of α, then the coordinates (x_i, y_i) of the nodes of the polygons can be expressed as follows:

$$x_i = \begin{cases} R\,cos\left(\frac{2\pi}{N} i\right), & for\ i = 1,2,\dots,6\ (bottom\ polygon) \\ R\,cos\left(\frac{2\pi}{N}(i - N) + \alpha\right), & for\ i = 7,8,\dots,12\ (top\ polygon) \end{cases}, \qquad 2.4$$

$$y_i = \begin{cases} R\,sin\left(\frac{2\pi}{N} i\right), & for\ i = 1,2,\dots,6\ (bottom\ polygon) \\ R\,sin\left(\frac{2\pi}{N}(i - N) + \alpha\right), & for\ i = 7,8,\dots,12\ (top\ polygon) \end{cases}, \qquad 2.5$$

where R is the radius of the circle that circumscribes both polygons and N is the number of sides of the polygons. Substituting the corresponding values of equations 2.4 and 2.5 into equation 2.3, the height of the structure can be expressed as:

$$H = \sqrt{L_b{}^2 + 2R^2(\cos\left(\frac{\pi}{3}\right)\cos\left(\frac{\pi}{3} + \alpha\right) + \sin\left(\frac{\pi}{3}\right)\sin\left(\frac{\pi}{3} + \alpha\right) - 1)}. \qquad 2.6$$

The height can be nondimensionalized by letting $\overline{L_b} = \frac{L_b}{b}$ and $\bar{R} = \frac{R}{b}$, where b is the width of the bar. Hence, the nondimensional height can be expressed as:

$$\bar{H} = \sqrt{\overline{L_b}^2 + 2\bar{R}^2(\cos\left(\frac{\pi}{3}\right)\cos\left(\frac{\pi}{3} + \alpha\right) + \sin\left(\frac{\pi}{3}\right)\sin\left(\frac{\pi}{3} + \alpha\right) - 1)}, \qquad 2.7$$

where $\overline{H} = \frac{H}{b}$.

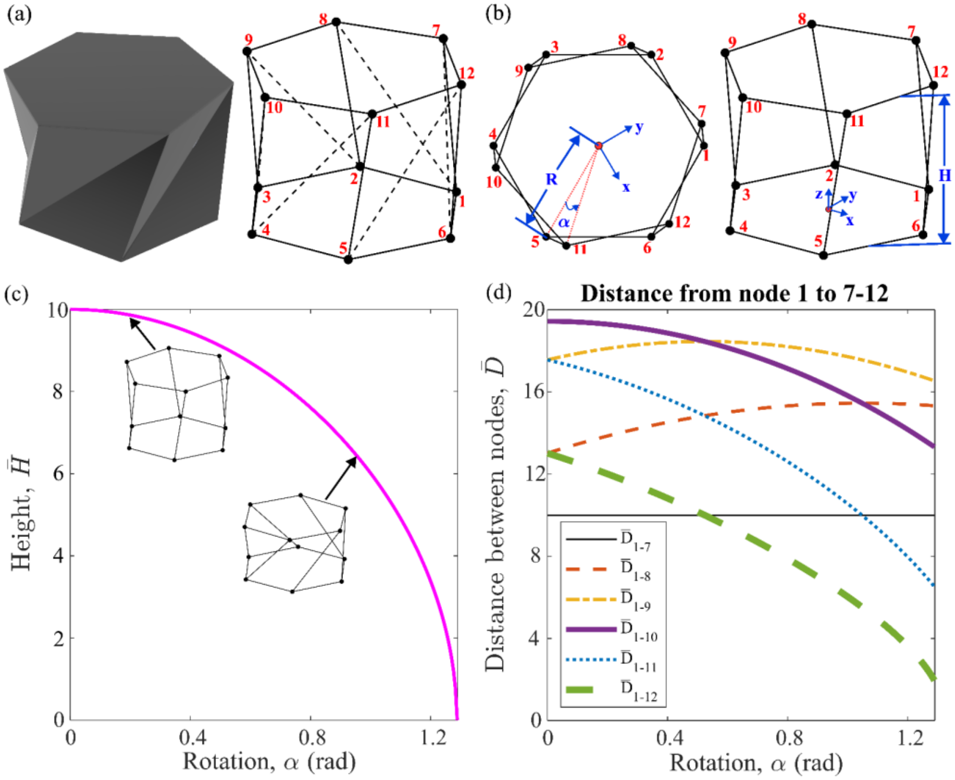

Figure 1. (a) A 3D model and schematic of a Kresling origami unit cell. (b) Top and isometric view of the design concept of the proposed kresling origami-inspired unit cell with pin jointed bars that are allowed to freely rotate as the structure is being deployed. (c) Relationship between the height and rotational angle of the unit cell during deployment. (d) Distance between node 1 and all the nodes of the top polygon during deployment.

With the previously defined parameters and for fixed values of R and L, the relationship between the height of the structure and the rotational angle α is illustrated in Figure 1c. Lastly, it is important to note that due to the symmetry of the structure, the distance from each of the bottom nodes to that all of the top 6 nodes is the same. For example, the distance between node 1 and 8 is the same as that from node 2 to 9. Hence, we will only show the distance between node 1 and the nodes 7 to 12. This distance can be defined as a function of α as follows:

$$D_{1-i} = \sqrt{(x_i - x_1)^2 + (y_i - y_1)^2 + H^2}\ , \quad for\ i = 7,8,9,\ldots,12. \qquad 2.7$$

The distance between the nodes can be nondimensionalized as follows:

$$\overline{D_{1-\imath}} = \sqrt{2\bar{R}^2\left(1-\cos\left(\frac{\pi}{3}\right)\cos\left(\frac{2\pi}{6}(i-6)+\alpha\right)-\sin\left(\frac{\pi}{3}\right)\sin\left(\frac{2\pi}{6}(i-6)+\alpha\right)\right)+\bar{H}^2}\ ,\ \ for\ i = 7,8,9,\ldots,12, \tag{2.8}$$

where $\overline{D_{1-\imath}} = \frac{D_{1-i}}{b}$. The distance between each of the nodes from above is plotted in Figure 1d as a function of α. As expected, the value from node 1 to 7 remains constant (rigid bar) for all values of α. The distance between the other nodes has distinct behaviors as the structure collapses. If tensile elements are connected between them, rich deformation behaviors can be obtained from the strings as heights changes.

In the previous work that implemented strings in a Miura-origami unit cell, bistability was realized by having energy contribution from the folding of the creases and the stretching of the strings [79]. The energy contribution of the string was controlled by appropriately selecting its unstretched length (defined to be the precise string length between the “slacked” and “tensioned” configurations). That is, the energy of the string contributes to the total energy of the system only when its current length is greater or equal than its unstretched length. It was observed that bistability was generated because near the vicinity of both stable states the energy contribution of the string was decreasing and that of the crease was increasing. From this observation, and with the rich kinematics of the Kresling origami-inspired structure, we can achieve multiple stable configurations in a single unit cell by exploiting the use of multiple tensile elements. To demonstrate this, we will first focus on the case of $N = 6$. As it is illustrated in Figure 1d, as the unit cell is deployed we have 3 pairs of nodes (1 to 10, 1 to 11 and 1 to 12) whose distance decreases as α increases and 2 pair of nodes (1 to 8 and 1 to 9) whose distance increases and decreases at different rates as α increases. To achieve the desired behavior, we can select one of the three whose length decreases (1 to 10, 1 to 11 or 1 to 12) and the two whose length increases and decreases at different rates. More specifically, if we add tensile elements between nodes 1 to 8, 1 to 9, and 1 to 11, and assume that there are no other strain energy storage elements at the joints/creases, we can obtain two distinct values of α where we have two strings (that are stretched, denoted by the bold line in the graph of Figure 2a) with opposing changes in length. Hence, we have two potential values of α where a stable configuration can be achieved, denoted by the light green boxes in the graph of Figure 2a. That is, around $\alpha = 0.4\ rad$, we can achieve a stable configuration by using the blue (decreasing in length) and the yellow string (increasing in length). Similarly, around $\alpha = 1\ rad$, we can achieve a stable configuration by using the yellow (now decreasing in length) and the orange string (increasing in length). We can increase the number of values of α that have this behavior by increasing the number of sides of the polygons, as we are increasing the number of nodes that can be used to connect more strings. By increasing the number of nodes in the top and bottom polygons of the unit cell (Figure 2), we can increase the number of regions of α with strings whose length changes are opposite. As shown in Figure 2b and c, for the cases of $N = 8$ and $N = 10$, we observe that the number of regions of α where the number of stable configurations can be realized increases to 3 and 4 (identified by the light green boxes), respectively.

Now that we have devised a strategy for realizing multiple stable configurations from the kinematics of the Kresling origami-inspired unit cell, the next step is to better understand the effect of the design parameters of the tensile elements on its multistability.

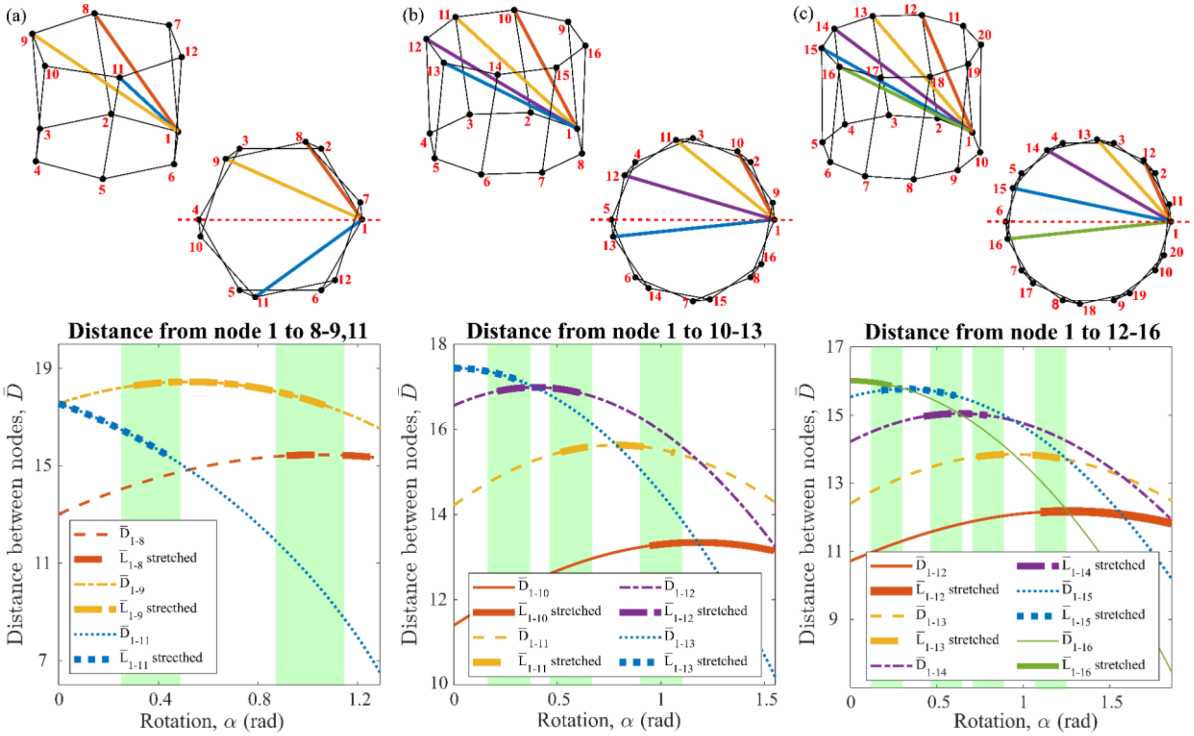

Figure 2. (a-c) Isometric and top view of the proposed unit cell with the distance between the specified nodes as function of α for distinct number of sides of the polygons: (a) N = 6, (b) N = 8, (c) N = 10. For all plots, the thin lines represent the distance between the specified nodes and the bold lines represent the potential regions where the strings will be in tension. The green light boxes represent the regions of α where a stable configuration can be realized by having two distinct strings with opposing changes in length.

Section 3: Design of the multistable unit cell

In this section, we present the methodology for the design of an eight-sided Kresling origami-inspired unit cell. Section 3.1 contains a detailed description of the modeling of the elastic elements of the unit cell. More specifically, the potential energy of the unit cell is equal to the sum from the energy contribution from the stretching of the strings and the folding of the creases. In Section 3.2 we study the effects of the design parameters on the multistability of the unit cell, for the folding range of the unit cell presented in Section 2. For the proposed eight-sided Kresling origami unit cell, we show that up to five stable configurations can be achieved. Furthermore, we present the experimental results for the tristable unit cell. Lastly, in Section 3.3 we expand the folding range of the unit cell and show that by doing this we can achieve up to ten stable configurations.

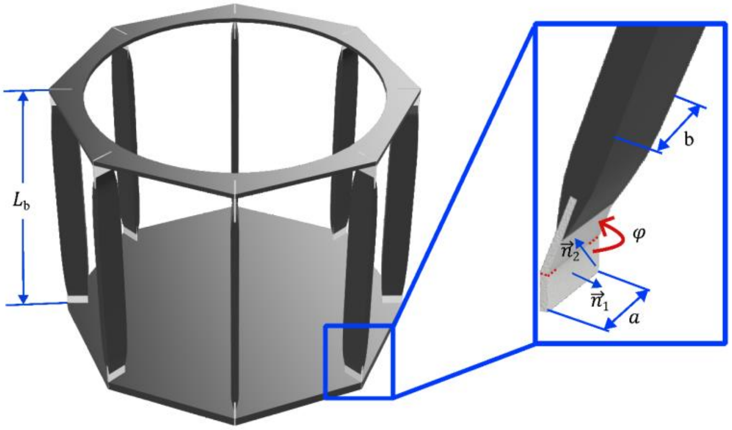

Figure 3. Design of the Kresling origami-inspired unit cell with rigid bars that are connected to the top and bottom polygons with thin elastic creases. The length and width of the bar are identified with L_b and b, respectively. The width and rotational angle of the creases are identified with a and φ, respectively.

To demonstrate the multistability of the proposed Kresling origami-inspired unit cell, we select the eight-sided polygon ($N = 8$) illustrated in Figure 3. The connection between the bars and polygons is simplified with a thin elastic crease at the connecting boundary that has a thin cut at the edges of the folding line of the crease (identified with red dashed line near the folding line of the crease in Figure 3). For the theoretical results presented in this section, the circumscribed radius (R) of the top and bottom polygon is 50 mm, the length (L_b) and width (b) of the bars is 70 mm and 7 mm, respectively, and the width of the creases (a) is 5 mm. It is assumed that the strings do not change the deformation path of the unit cell and that there is no contact between them.

3.1. Mechanics of the unit cell

The material of the tensile elements and creases is assumed to be linearly elastic. From the rigid bar assumption, the total potential energy of the unit cell is equal to the sum of the potential energy from the tensile elements and the creases. That is:

$$\Pi = \Pi_{string} + \Pi_{crease}. \qquad 3.1$$

The potential energy of the string can be calculated as follows:

$$\Pi_{string} = \begin{cases} N_s\left(\frac{1}{2}k_s(L(\alpha) - L_o)^2\right), & for\ L(\alpha) \geq L_o \\ 0, & for\ L(\alpha) < L_o \end{cases}, \qquad 3.2$$

where k_s is the axial stiffness of the string, N_s is the number of strings in the unit cell, and $L(\alpha)$ and L_o are the current length and the unstretched length of the string, respectively. The potential energy of the string is equal to that of a linear spring when its current length is greater than its unstretched length and equal to zero when the current length is less than its unstretched length. The axial stiffness is equal to:

$$k_s = \frac{EA}{L_o}, \qquad 3.3$$

where E and A are the young's modulus cross sectional area of the string, respectively. It will be assumed that all strings are made of the same elastic material and have the same diameter. Hence, EA is the same for all strings. The creases are assumed to be thin elastic hinges that can be modeled as torsional springs. Hence, the total potential energy of the creases is:

$$\Pi_{crease} = N_c \left(\frac{1}{2} k_\varphi a (\varphi(\alpha) - \varphi_o)^2\right), \qquad 3.4$$

where k_φ is the torsional elastic constant, a is the width of the crease, N_c is the total number of creases, $\varphi(\alpha)$ and φ_o are the current angle (illustrated in Figure 3) and the stress-free state of the crease, respectively. The angle of the crease can be calculated from the normal $(\overrightarrow{n_1}, \overrightarrow{n_2})$ of each panel adjacent to the crease as follows:

$$\varphi(\alpha) = cos^{-1}\left(\frac{\overrightarrow{n_1} \cdot \overrightarrow{n_2}}{|\overrightarrow{n_1}| \cdot |\overrightarrow{n_2}|}\right). \qquad 3.5$$

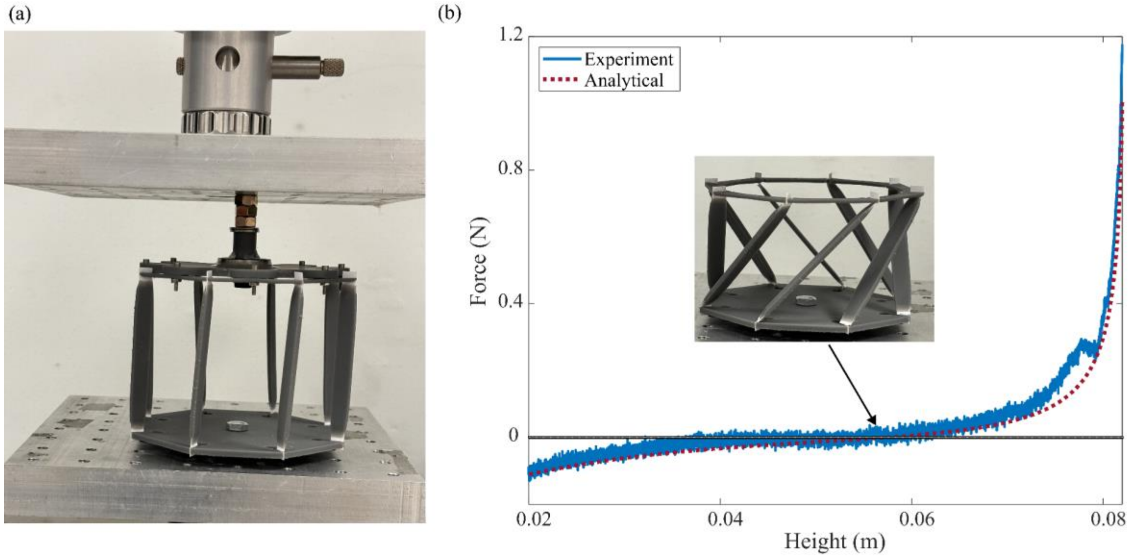

Figure 4. (a) Experimental setup of the unit cell in the tensile machine (Instron 5965). (b) Force-displacement profiles of the unit cell for the experiment (blue solid line) and analytical model (red dash line) without strings, with the identified stable state of the protype.

The proposed analytical model of a unit cell with creases (but without strings) is validated experimentally. The prototype is composed of creases made of cardstock paper [50,80] and the rest of the components were 3D printed (Formlabs 3) with stereolithography (SLA) resin. Figure 4a shows the experimental setup of the unit cell in the tensile test machine (Instron 5965). The top polygon of the unit cell was attached to the moving section of the tensile test machine and the bottom polygon was attached to the fixed section of the machine. Since the machine can only apply translational displacement, the unit cell was connected to the top part using a ball bearing that couples its translational and rotational motion. Using the value of $k_{\varphi} = 170x10^{-3}$ for cardstock paper [50,80], the theoretical force-displacement was calculated using $F_{creases} = \frac{d\Pi_{creases}}{dH}$. The results show good agreement between the analytical model and experiments, illustrated in Figure 4b.

3.2. Classic folding of Kresling origami

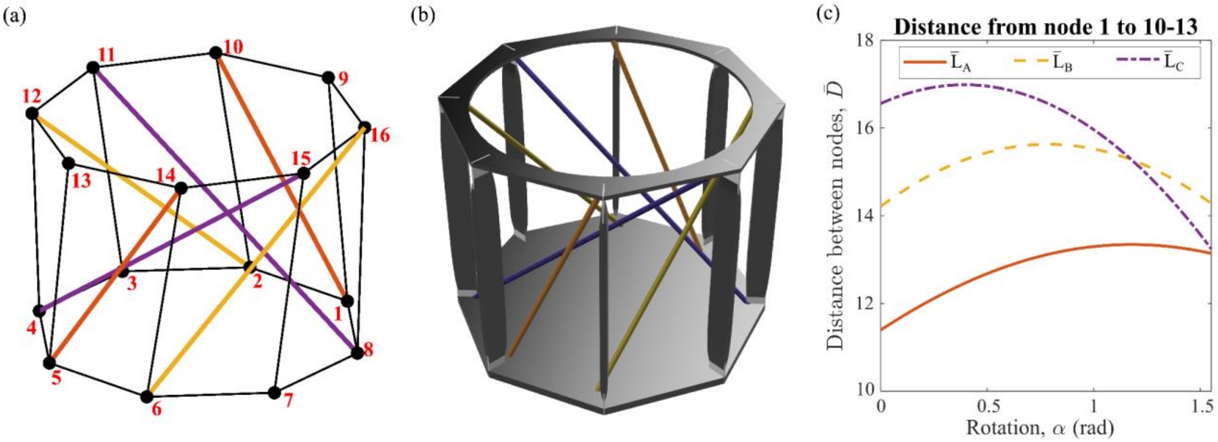

Figure 5. (a) Schematic and (b) 3D model of the proposed unit cell with the three distinct (two of each) strings, identified in orange, yellow and purple. (c) Distance between the nodes of the unit cell for strings A (orange solid line), B (yellow dash line) and C (purple dot and dash line) as the structure is being deployed.

Next, we will study the effect of the design parameters of the unit cell on its multistability by focusing on the classical rotational motion of Kresling. The triangular panels of this origami pattern constrain the unit cell to only rotate (starting from $\alpha = 0$) for the range of $\alpha > 0$ or $\alpha < 0$. In contrast, since the proposed Kresling origami-inspired unit cell is composed of bars that are allowed to freely rotate at its joints, it can cover both the negative and positive values of α. In this subsection, we will focus on the range of $\alpha \geq 0$. To achieve the desired string deformation behavior presented in Section 2, the unit cell has a total of six strings where three of them have distinct deformation behaviors as α changes. The tensile elements of the unit cell are identified as string A (two, from node 1 to 10 and 5 to 14), string B (two, from node 2 to 12 and 6 to 16) and string C (two, from 4 to 15 and 8 to 11), all illustrated in Figure 5. It is important to emphasize that due to the symmetry of the unit cell (discussed in Section 2), the distance between the nodes selected for strings A, B and C are the same to that between nodes 1 to 10, 1 to 11 and 1 to 12, respectively. The total potential energy of the system is equal to:

$$\Pi = N_{sA}\left(\frac{1}{2}k_{sA}(L_A(\alpha) - L_{oA})^2\right) + N_{sB}\left(\frac{1}{2}k_{sB}(L_B(\alpha) - L_{oB})^2\right) + N_{sC}\left(\frac{1}{2}k_{sA}(L_A(\alpha) - L_{oA})^2\right) + N_c\left(\frac{1}{2}k_{\varphi}a(\varphi(\alpha) - \varphi_o)^2\right), \quad 3.6$$

where $N_{sA} = N_{sB} = N_{sC} = 2$, $N_c = 16$ and the length of each string can be calculated as follows:

$$\begin{aligned} L_A &= \sqrt{(x_{10} - x_1)^2 + (y_{10} - y_1)^2 + H^2} \\ &= \sqrt{(x_{14} - x_5)^2 + (y_{14} - y_5)^2 + H^2}\,, \end{aligned} \tag{3.7}$$

$$\begin{aligned} L_B &= \sqrt{(x_{12} - x_2)^2 + (y_{12} - y_2)^2 + H^2} \\ &= \sqrt{(x_{16} - x_6)^2 + (y_{16} - y_6)^2 + H^2}\,, \end{aligned} \tag{3.8}$$

$$\begin{aligned} L_C &= \sqrt{(x_{15} - x_4)^2 + (y_{15} - y_4)^2 + H^2} \\ &= \sqrt{(x_{11} - x_8)^2 + (y_{11} - y_8)^2 + H^2}\,, \end{aligned} \tag{3.9}$$

$$H = \sqrt{{L_b}^2 - (x_9 - x_1)^2 - (y_9 - y_1)^2}. \tag{3.10}$$

Following a similar procedure to the one presented in Section 2, the length of the strings and the height of the structure can be nondimensionalized by letting $\overline{L_b} = \frac{L_b}{b}$ and $\bar{R} = \frac{R}{b}$. The nondimensional form of equations 3.7 to 3.10 can be expressed as follows:

$$\bar{L}_A = \sqrt{2\bar{R}^2\left(1 - \cos\left(\frac{\pi}{4}\right)\cos\left(\frac{\pi}{2} + \alpha\right) - \sin\left(\frac{\pi}{4}\right)\sin\left(\frac{\pi}{2} + \alpha\right)\right) + \bar{H}^2}\,, \tag{3.11}$$

$$\bar{L}_B = \sqrt{2\bar{R}^2\left(1 - \cos\left(\frac{\pi}{2}\right)\cos(\pi + \alpha) - \sin\left(\frac{\pi}{2}\right)\sin(\pi + \alpha)\right) + \bar{H}^2}, \tag{3.12}$$

$$\bar{L}_C = \sqrt{2\bar{R}^2\left(1 - \cos(\pi)\cos\left(\frac{7\pi}{4} + \alpha\right) - \sin(\pi)\sin\left(\frac{7\pi}{4} + \alpha\right)\right) + \bar{H}^2}\,, \tag{3.13}$$

$$\bar{H} = \sqrt{\overline{L_b}^2 + 2\bar{R}^2\left(\cos\left(\frac{\pi}{4}\right)\cos\left(\frac{\pi}{4} + \alpha\right) + \sin\left(\frac{\pi}{4}\right)\sin\left(\frac{\pi}{4} + \alpha\right) - 1\right)}, \tag{3.14}$$

where $\bar{L}_A = \frac{L_A}{b}$, $\bar{L}_B = \frac{L_B}{b}$, $\bar{L}_C = \frac{L_C}{b}$ and $\bar{H} = \frac{H}{b}$. The total potential energy can be nondimensionalized by letting $\bar{L}_{oA} = \frac{L_{oA}}{b}$, $\bar{L}_{oB} = \frac{L_{oB}}{b}$, $\bar{L}_{oC} = \frac{L_{oC}}{b}$, $\bar{a} = \frac{a}{b}$, and $\bar{K} = \frac{k_\varphi}{EA}$. Hence, the nondimensionalized equation of potential energy is equal to:

$$\bar{\Pi} = N_{sA}\left(\frac{1}{2\bar{L}_{oA}}(\bar{L}_A - \bar{L}_{oA})^2\right) + N_{sB}\left(\frac{1}{2\bar{L}_{oB}}(\bar{L}_B - \bar{L}_{oB})^2\right) + N_{sC}\left(\frac{1}{2\bar{L}_{oC}}(\bar{L}_C - \bar{L}_{oC})^2\right) + N_c\left(\frac{1}{2}\bar{a}\bar{K}(\varphi(\alpha) - \varphi_o)^2\right), \quad 3.15$$

where $\bar{\Pi} = \frac{\Pi}{EAb}$. From the equation from above we know that the design variables are the unstretched length of the strings ($\bar{L}_{oA}$, $\bar{L}_{oB}$, $\bar{L}_{oC}$), the stress-free state of the creases (φ_o) and the ratio $\bar{K}$. Based on the principle of stationary potential energy, a stable configuration will be achieved at any specified value of α when the following criteria are met:

$$\frac{d\bar{\Pi}}{d\alpha} = 0, \qquad \frac{d^2\bar{\Pi}}{d\alpha^2} > 0. \quad 3.16$$

Using these criteria, we will study the effect of the five design variables on the number of stable configurations of the unit cell. The range of the unstretched length values of the string was selected as follows. The upper limit was the maximum length the string can achieve as the unit cell is deployed. The lower limit was calculated by solving for the minimum length that will yield a 2% strain when the string is stretched to its maximum length. The values of the stress-free state of the creases were strategically selected such that these were at three different heights (near maximum, middle and minimum height values of the unit cell).

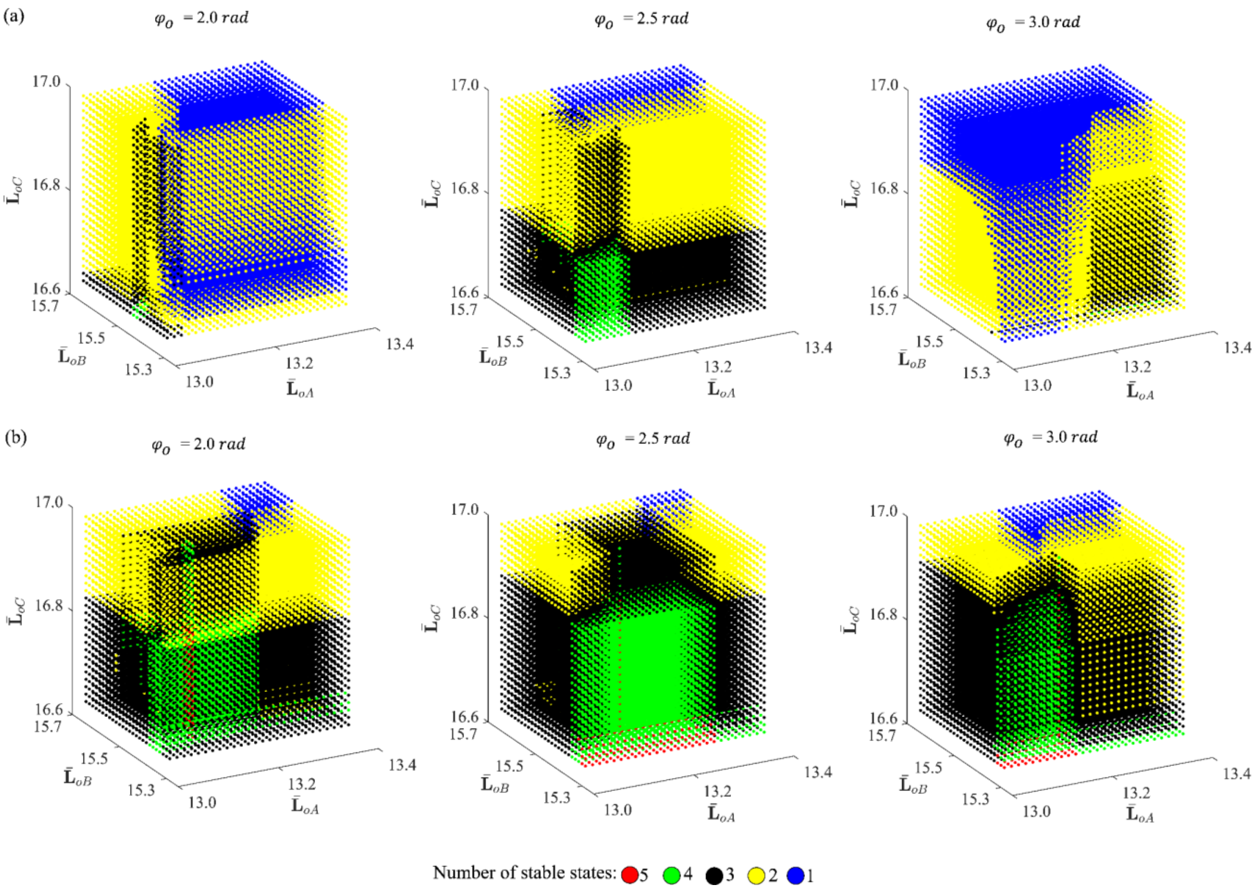

Figure 6. (a,b) Number of stable configurations that can be realized in a single unit cell for (a) $\bar{K} = 3.5x10^{-3}$ and (b) $\bar{K} = 1.0x10^{-3}$ for three values of the stress free state of the crease (2, 2.5 and 3 rad) for wide range of unstretched length value of the three distinct strings. Where the number of stable states are color coded from one stable state (blue) to five stable states (red).

To visualize this, Figure 6 shows the number of stable configurations that can be achieved for distinct combinations of the five design parameters. Figure 6a illustrates the case of $\bar{K} = 3.5x10^{-3}$ with the unstretched length values of the three distinct strings plotted for the respective values of stress-free state of the creases. For this ratio, the value of the crease stress-free state has a significant effect on the amount of distinct combinations of string unstretched length values that yield the same number of stable configurations. For $\varphi_o = 2.0\, rad$ and $\varphi_o = 3.0\, rad$, the maximum number of stable configurations that can be achieved is four, but with a limited number of combinations of string unstretched length. Most of the combinations of string unstretched length values will yield monostable and bistable designs (blue and yellow). For $\varphi_o = 2.5\, rad$, when compared to the previous two crease stress-free states, a significant number of distinct combinations of string unstretched length values will yield three and four stable configurations (identified with the black and green dots). Figure 6b illustrates the case of $\overline{K} = 1.0x10^{-3}$. For the three selected values of crease stress-free state up to five stable configurations can be achieved in a single unit cell. By reducing the value of $\overline{K}$ (reducing the energy contribution from the creases), the crease stress-free state value does not limit the amount of combinations that can be made to generate tristable and quadstable elements. To gain more insight on the effect of this design parameter on the number of stable configurations, the maximum number of stable configurations that can be achieved in a single unit cell were calculated for a specified range of $\overline{K}$ with $\varphi_o = 2.5\, rad$ and the same set of properties for the strings. Figure 7 shows that when this value is equal or less than $\overline{K} = 2.5x10^{-3}$, then the unit cell can achieve up to five stable configurations. Hence, as the ratio between the torsional elastic constant of the creases and the tensile force of the string decreases, more stable states can be achieved with different combinations of string unstretched length and crease stress-free state.

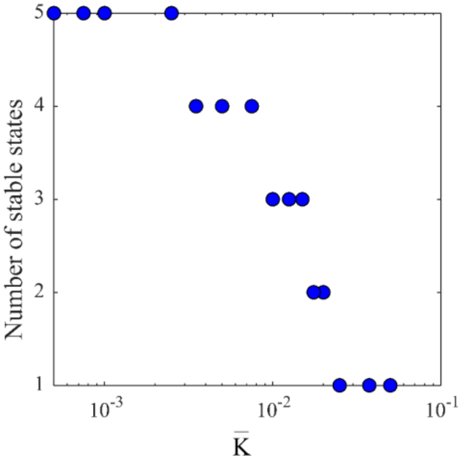

Figure 7. Maximum number of stable configurations that can be realized in a single unit cell for different values of $\overline{K}$.

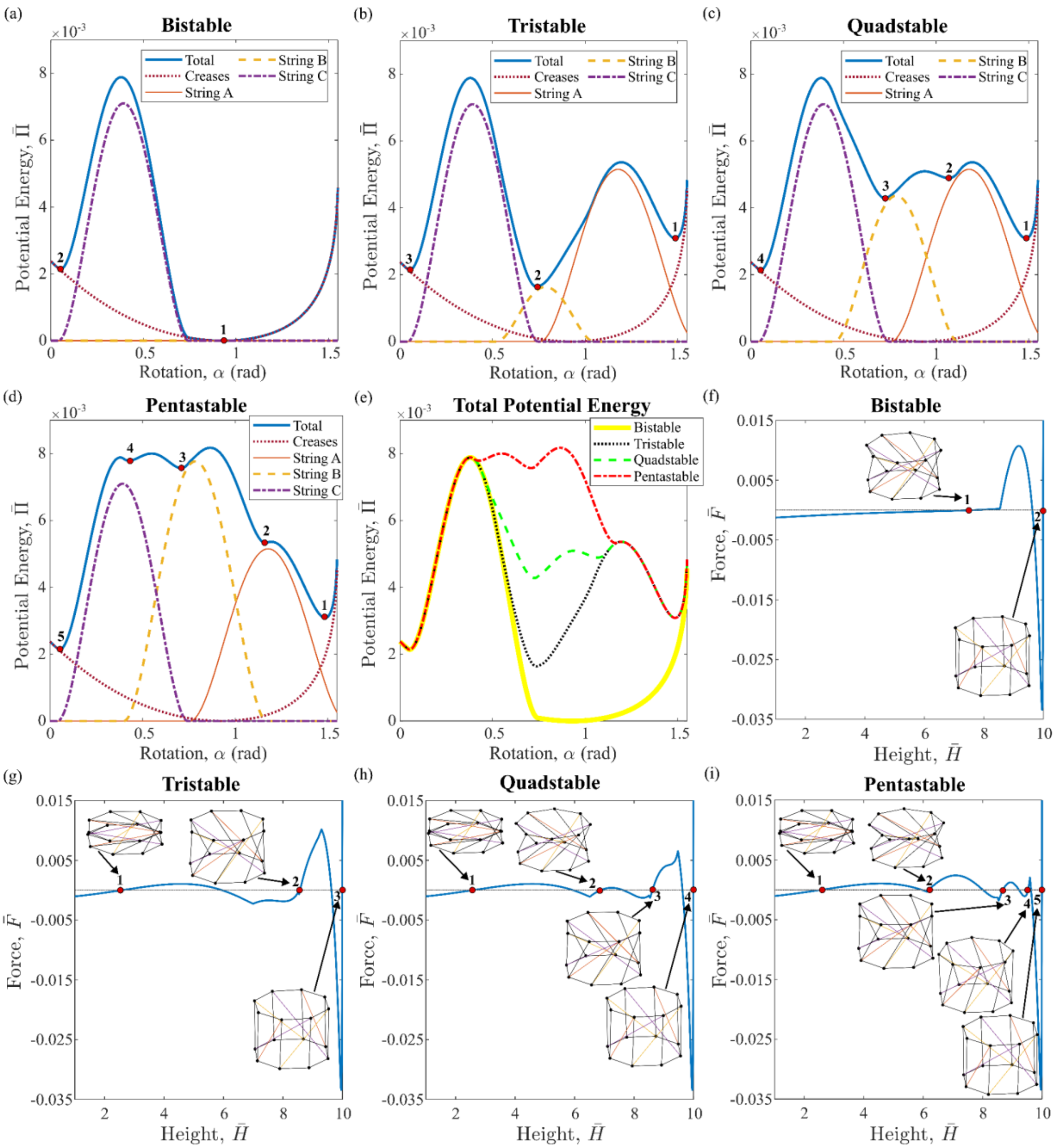

Figure 8. (a-d) The total potential energy profile for the cases from bistable to pentastable with the identified values of α for the stable states and the contribution from the three distinct strings and the creases. (e) Potential Energy landscape for different stable configurations. (f-i) Force-Displacement profiles for the corresponding stable cases from (a-d), along with the identified height values of each stable state.

Next, we show and discuss the potential energy profile and force-displacement relationship for the bistable, tristable, quadstable and pentastable unit cells. Figure 8a-d shows the total potential energy plot of the system, along with the energy contribution of each of the strings and the creases. The red dots in these plots indicate the value of α with a stable state. The total potential energy profiles are obtained from equation

3.11, for $\bar{K} = 1.0x10^{-3}$ and $\varphi_o = 2.5\,rad$. To realize the bistable unit cell, only string C needs to be stretched with a nondimensional unstretched length value of 16.6429 (dimensional value of 116.5 mm), while strings A and B remain slack. For the tristable, quadstable and pentastable cases the nondimensional unstretched length of string C was the same as the bistable case and the nondimensional unstretched length of string A was selected to be 13.0857 (91.6 mm). The difference between all the number of stable states in each case is the unstretched length value of string B. For the tristable, quadstable and pentastable the nondimensionalized string unstretched length values are 15.4714 (108.3 mm), 15.3714 (107.6 mm) and 15.2857 (107 mm), respectively. This demonstrates that the multistability of the unit cell can be easily tuned by adjusting the unstretched length of one string. The effect of the change in the potential energy profile for the different stable configurations is shown in Figure 8e. Figure 8f-i shows the corresponding force-displacement plot for each of the multistable unit cells, which is calculated using $F = \frac{d\bar{\Pi}}{d\bar{H}}$. The red dots indicate the height value of the unit cell at which each of the stable configurations is realized.

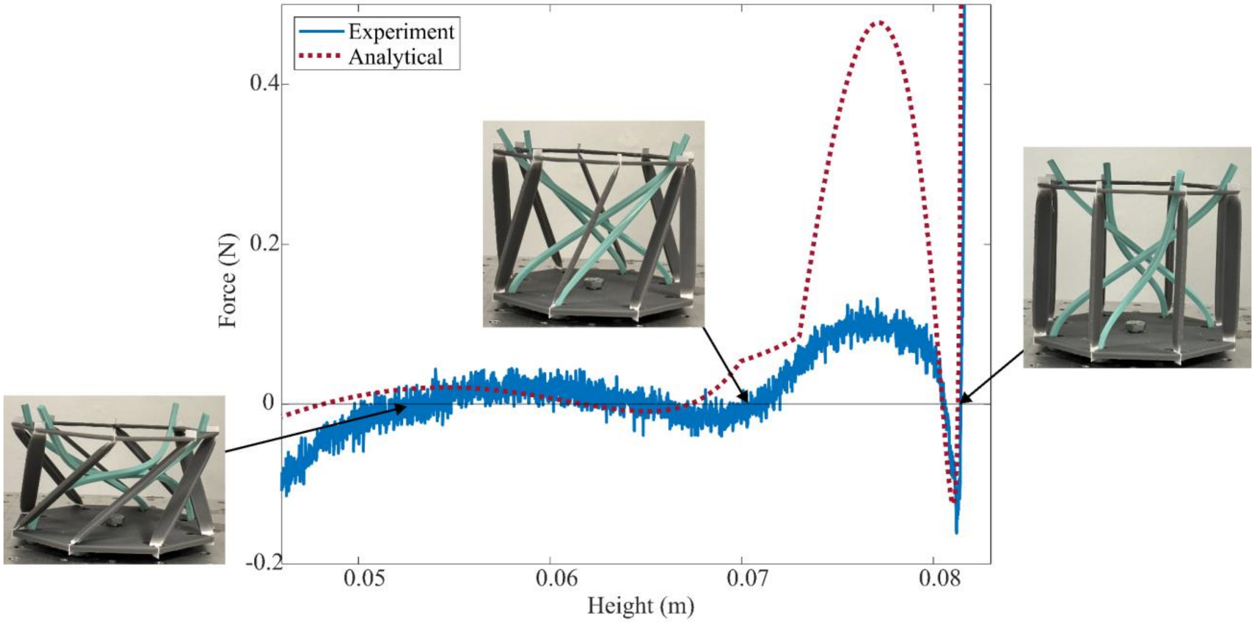

Figure 9. Force-displacement profile for the experiment (solid blue line) and analytical model (red dash line). With the identified stable states of the prototype.

Lastly, elastic strings (made out of silicone rubber, Smooth Sil 960 [81]) are attached to the experimental prototype presented in Section 3.1. Strings A and C are added to the structure and their corresponding set of unstretched length values are used to realize three stable configurations. Using the value of $E = 2.88\ MPa$ for Smooth Sil 960 [81], the analytical force-displacement profile was obtained using $F = \frac{d\Pi}{dH}$. Figure 9 illustrates the corresponding analytical and experimental force-displacement results. These show good agreement at the location of the stable configuration of maximum height and an offset of approximately 4 mm at the other two stable configurations. A potential reason for this difference could be due to manufacturing imperfections that cause the deformation path of the strings to vary from that of the analytical model. Additionally, there are discrepancies with some of the force magnitudes, specifically between the heights of 70 and 80 mm. A potential reason for the deviation of the force-displacement profile could be attributed to the fact that strings of the prototype with the higher energy contribution in this region have some level of curvature and in the analytical model these are assumed to be perfectly straight. The curvature of the physical strings causes their energy contribution to be less than the one expected from the analytical model, creating this offset in the force displacement plot near the region between the heights of 70 and 80 mm. Nevertheless, the experiments have shown that we can realize three stable configurations in the unit cell by the strategic integration of tensile elements, as predicted by the analysis.

3.3. Beyond the folding of Kresling origami

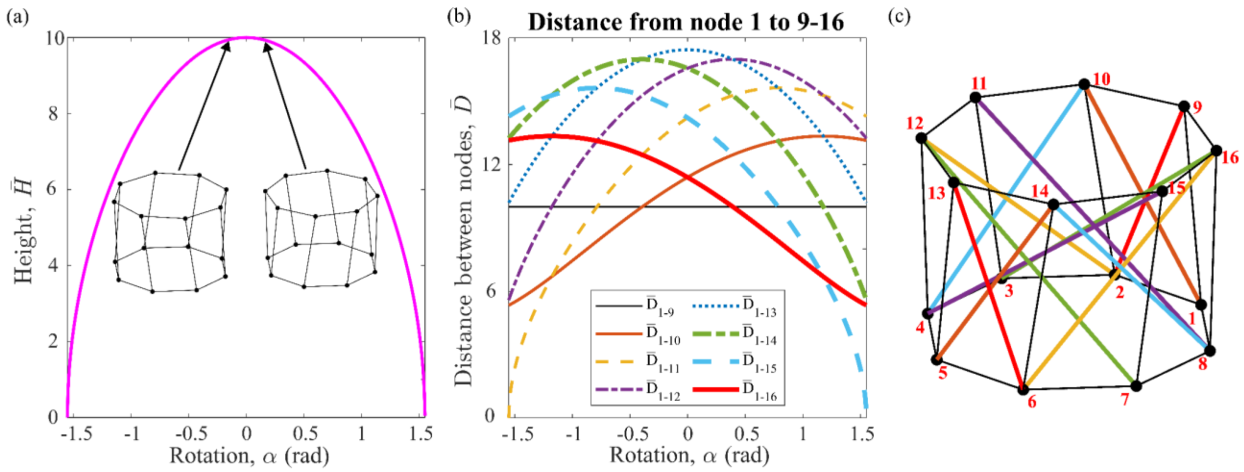

Figure 10. (a) Height profile of the unit cell and (b) distance between its nodes for the entire range of α. (c) Schematic of the unit cell with all of its strings.

As mentioned in the previous subsection, since the proposed Kresling-inspired unit cell is composed of bars and strings, it can go beyond the folding capabilities of Kresling. When folded, it can cover the range of $\alpha \geq 0$ and $\alpha < 0$. This leads the unit cell to have the same height profile with two distinct rotational paths (or the same height value for two distinct values of α), as illustrated in Figure 10a. Additionally, the distance between the nodes in the unit cell is shown in Figure 10b for the entire range of α. For the range of negative values of α, the increasing and decreasing behavior of the distance between the nodes (as the structure is deployed) occurs between different nodes than that of the positive range. That is, the three strings (used in Section 3.2) that are placed between nodes 1 and 10, 1 and 11 and 1 and 12 are mirrored at $\alpha = 0$ by that of nodes 1 to 16, 1 to 15 and 1 to 14 (illustrated in Figure 10b). This allows us to utilize the strategy from Section 3.2 for the negative values of α. Since the nodes utilized for the negative range of α mirrors that of the values of the positive range of α, the unit cell can be designed to realize the same height value for two distinct values of α by using the same set of mirrored strings. It is important to note that although these values are mirrored, they are still between different nodes, which enables the realization of distinct height values for the same set of mirrored strings. Hence, the broad design space of the unit cell leads to a highly programmable unit cell. To validate this, we add the energy terms of the "new" strings (1 to 14, 15, 16) to the unit cell. The added tensile elements of the unit cell are identified as string D (two, from node 7 to 12 and 3 to 16), string E (two, from node 4 to 10 and 8 to 14) and string F (two, from 2 to 9 and 6 to 13). All identified in Figure 10c, along with the other strings from Section 3.2. For this case study, the tensile force of the strings D, E and F is assumed to be two times the value of the tensile force of the strings A, B and C. Hence, the nondimensional potential energy equation from Section 3.2 as follows:

$$\begin{aligned}\bar{\Pi} = \bar{\Pi}_{+\alpha} + N_{sD}\left(\frac{1}{\bar{L}_{oD}}(\bar{L}_D - \bar{L}_{oD})^2\right) + N_{sE}\left(\frac{1}{\bar{L}_{oE}}(\bar{L}_E - \bar{L}_{oE})^2\right) \\ + N_{sF}\left(\frac{1}{\bar{L}_{oF}}(\bar{L}_F - \bar{L}_{oF})^2\right),\end{aligned} \qquad 3.17$$

where $\bar{\Pi} = \frac{\Pi}{EAb}$, $\bar{\Pi}_{+\alpha}$ is the four terms from equation 3.15, $\bar{L}_D = \frac{L_D}{b}$, $\bar{L}_{oD} = \frac{L_{oD}}{b}$, $\bar{L}_E = \frac{L_E}{b}$, $\bar{L}_{oE} = \frac{L_{oE}}{b}$, $\bar{L}_F = \frac{L_F}{b}$, $\bar{L}_{oF} = \frac{L_{oF}}{b}$. From this equation we know that design variables are the nondimensional unstretched length values of the added strings ($\bar{L}_{oD}$, $\bar{L}_{oE}$, $\bar{L}_{oF}$). Similar to the procedure from subsection 3.2, for fixed values of $\bar{K} = 1x10^{-3}$, $\varphi_o = 2.5\,rad$, $\bar{L}_{oA} = 13.0857$, $\bar{L}_{oB} = 15.2857$, and $\bar{L}_{oC} = 16.6429$, and by using the criteria from equation 3.16 we can better understand the effect of the design variables on the number of stable configurations of the unit cell. This is shown in Figure 11a, where a maximum of 10 stable configurations can be realized in a single unit cell. Figure 11b shows the total potential energy landscape of the decastable unit cell and Figure 11c shows the force-displacement curves for the positive and negative values of α. Hence, by exploiting the entire range of α we can achieve up to 10 stable configurations in a single unit cell.

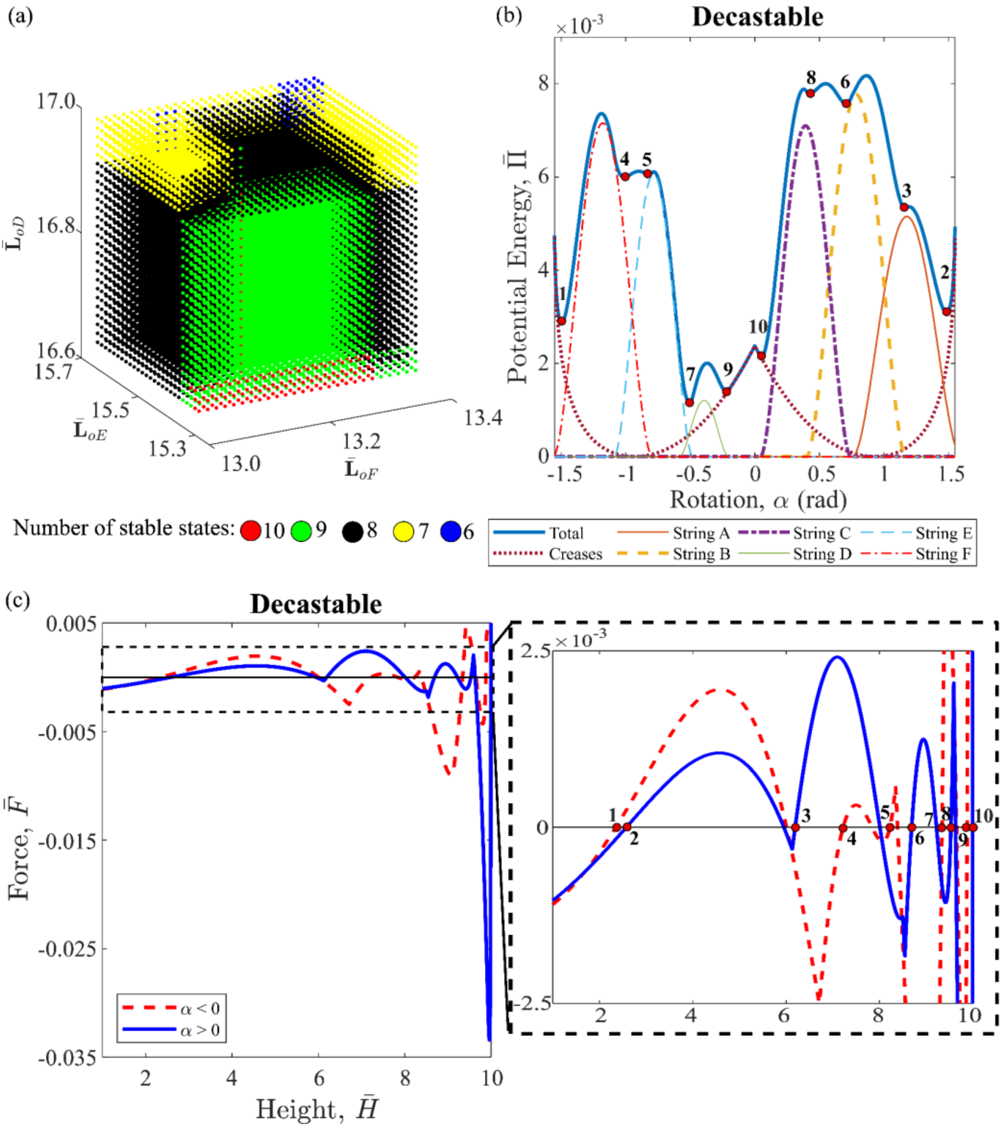

Figure 11. (a) Number of stable configurations that can be realized with distinct combination of unstretched length values of the three new distinct strings. Where the number of stable states if color coded from six stable states (blue) to ten stable states (red). (b) Potential energy landscape and c) Force-displacement profile for the decastable unit cell, with the corresponding stable configurations identified with the red dots.

Lastly, an experimental prototype is tested to demonstrate the feasibility of realizing multiple stable configurations by exploiting the positive and negative values of α. In this study, we used commercially available strings made out of rubber fibers that are covered by polyester fabric. By adding string E to the same unit cell of subsection 3.2, five stable configurations were realized. Figure 12 shows the experimental force-displacement profiles for the positive (thin red line) and negative (thick blue line) range of α, along with snapshot of the unit cell at their corresponding stable state.

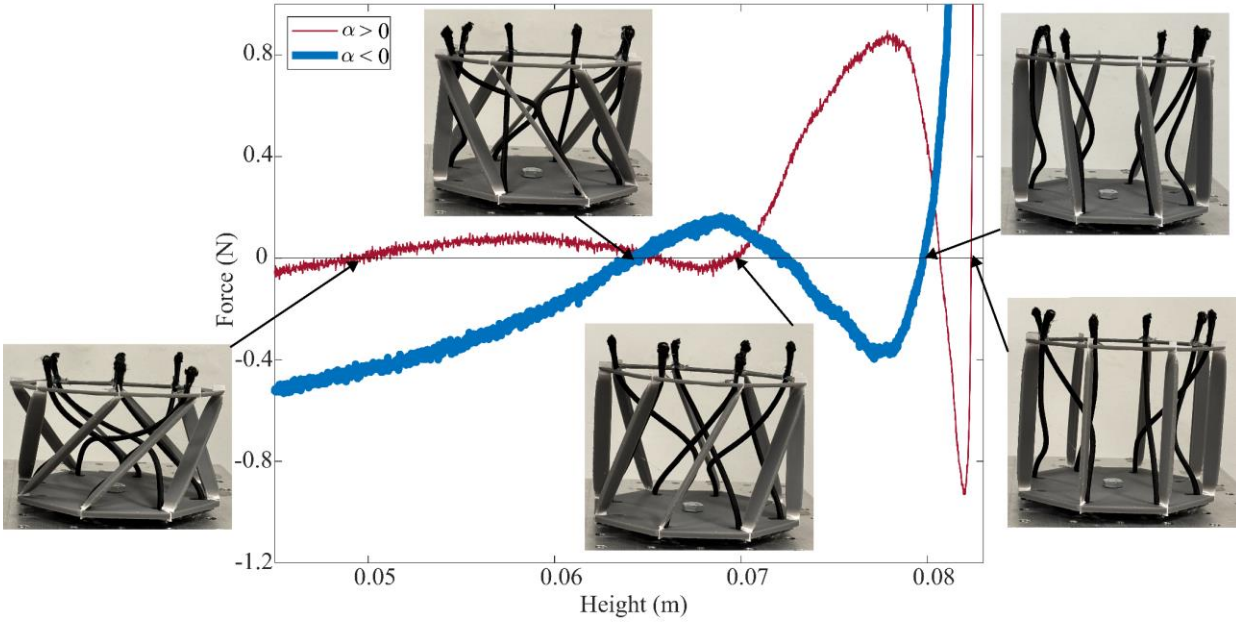

Figure 12. Experimental force-displacement profiles for the positive (thick blue line) and negative (thin red line) values of α, with the identified stable configurations of the prototype.

Section 4: Effects of increasing the number of stable states per unit cell for property tuning

In this section, we present the advantages of having multiple stable configurations in a single unit cell for mechanical property tailoring. We achieve this by using the multistable unit cells (from bistable to decastable) that were uncovered in Section 3. In Section 4.1 we show the case study of two unit cells assembled in series and present the effects on the number of equivalent stiffness values as we increase the number of stable states in each unit cell. More specifically, we show that by increasing the number of stable states in each unit cell we can significantly increase the total number of distinct values of equivalent stiffness. In Section 4.2 we study the effect on the number of bistable, tristable, quadstable and pentastable unit cells needed to achieve the same programmable capabilities of the decastable unit cell. We show that by having more stable configurations per unit cell significantly reduces the size and weight of the structure.

4.1. Equivalent stiffness model for two-unit cells in series

Table 1. Stiffness value at each stable configuration for the respective multistable unit cell.

	Nondimensional stiffness value at each stable state									
Number of stable states per unit cell	$\overline{K}_1$	$\overline{K}_2$	$\overline{K}_3$	$\overline{K}_4$	$\overline{K}_5$	$\overline{K}_6$	$\overline{K}_7$	$\overline{K}_8$	$\overline{K}_9$	$\overline{K}_{10}$
2	1.94x10^{-4}	5.952								
3	7.51x10^{-4}	0.0217	5.952							
4	7.51x10^{-4}	2.13x10^{-3}	0.0164	5.952						
5	7.51x10^{-4}	5.0x10^{-3}	0.01	0.0229	5.952					
10	1.06x10^{-3}	7.51x10^{-4}	5.0x10^{-3}	2.45x10^{-3}	3.05x10^{-3}	0.01	0.0573	0.0229	0.16	5.952

To evaluate the advantages of realizing more stable states per unit cell, we performed a case study on the programmable stiffness of two unit cells assembled in series. The two unit cells can be simplified to two springs in series as illustrated in Figure 13a. The equivalent stiffness is equal to:

$$\frac{1}{k_{eq}} = \frac{1}{{k_1}^{(i)}} + \frac{1}{{k_2}^{(j)}}, \tag{4.1}$$

$$k_{eq} = \frac{{k_1}^{(i)}{k_2}^{(j)}}{{k_1}^{(i)} + {k_2}^{(j)}}, \tag{4.2}$$

where ${k_1}^{(i)}$ and ${k_2}^{(j)}$ are the stiffness of the first and second unit cell, respectively. The subscripts i and j represent the stiffness value of the corresponding stable state for each unit cell. From the force-displacement results from Sections 3.2 and 3.3 we can derive the linear stiffness at each stable configuration by using $\overline{K} = \frac{d\overline{F}}{d\overline{H}}$. Table 1 summarizes the values of the stiffness of the unit cell at each stable configuration for the bistable, tristable, quadstable and pentastable and decastable unit cells. The total number of combinations (order does not matter and repetition is allowed) that can be realized for the two springs in series is equal to:

$$C = \frac{(n + r - 1)!}{r!\,(n - 1)!}, \tag{4.3}$$

where n is the number of stable states per unit and r is the number of unit cells assembled in series. For $r = 2$, Figure 13b shows the number of distinct values of equivalent stiffness (C) that can be realized for a range of stable states (n) per unit cell from 2 to 10. If the unit cell is bistable, the system will have 3 distinct values of equivalent stiffness, and if it is decastable it will have 55. Hence, when compared to the bistable unit, the decastable can achieve 52 more distinct equivalent stiffness values with the same weight and occupying the same volume. To illustrate this, we select the stiffness values from Table *1* for the bistable, tristable, quadstable, pentastable and decastable cases and plot it against the number of distinct values of stiffness for each of the stable configurations. Figure 13c illustrates the equivalent stiffness values (k_{eq}) that can be achieved for each of the number of stable states from Table 1. Realizing ten stable states per unit cell enables the system to have 55 distinct values of equivalent stiffness shown in Figure 13c. Hence, with the same number unit cells (same size, volume and weight) the decastable Kresling origami-inspired structure can achieve 52, 49, 45 and 40 more discrete values of equivalent stiffness than the bistable, tristable, quadstable and pentastable cases, respectively.

4.2. Increasing the number of unit cells

In parallel to the effect on the number of programmable distinct mechanical properties (e.g., stiffness), increasing the number of stable configurations per unit cell also has a significant impact on the size of the system. From the previous section, we know that two decastable unit cells in series yield 55 distinct values of stiffness. To match this number using bistable unit cell elements it will require 54 unit cells in series, as highlighted with the rectangular box with red border in Figure 13d. This is due to the fact that, for a bistable unit cell, increasing the number of unit cells causes a linear increment on the number of distinct values of equivalent stiffness. On the other hand, as the number of stable states per unit cell is increased beyond 2, this relationship becomes nonlinear (this is illustrated in Figure 13e for the cases of bistable, tristable, quadstable and pentastable unit cells). This nonlinear effect causes the number of unit cells needed to achieve the 55 distinct stiffness of the two decastable unit cells to reduce drastically, where the tristable cell requires 9 unit cells, the quadstable cell requires 5 unit cells, and the pentastable cell requires 4 unit cells. This shows that for achieving the same programmable capabilities, the system with the highest number of stable states per unit cell will have the fewest number of cells.

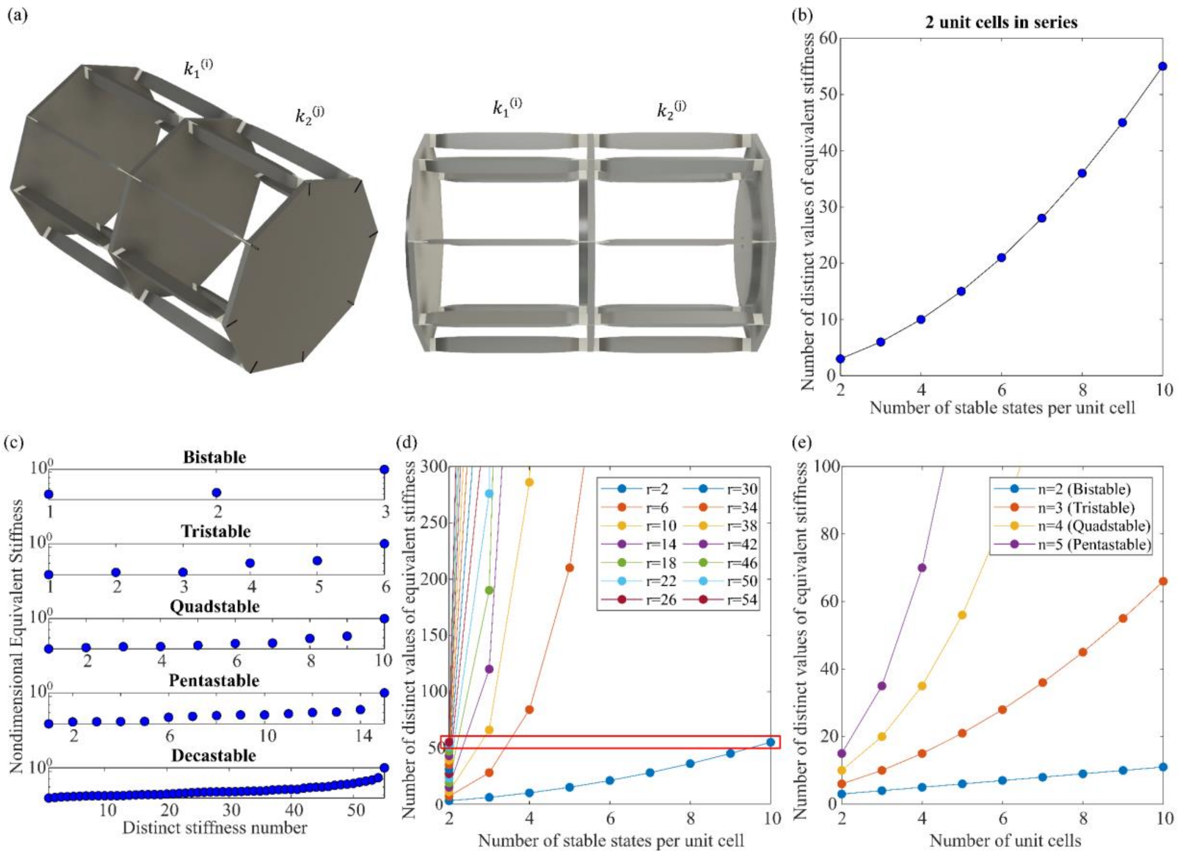

Figure 13. (a) Isometric and 2D view of two unit cells assembled in series (b) Total number of distinct values of equivalent stiffness as a function of the number of stable states per unit cell for the case of two unit cells in series. (c) Nondimensional values of stiffness for the cases of bistable, tristable, quadstable, pentastable and decastable. (d) Total number of distinct values of equivalent stiffness as a function of the number of stable states per unit cell for the range of the number of unit cells from r = 2 to 54 (with increments of 4) assembled in series. (e) Effect of increasing the number of unit cells on the number of distinct values of equivalent stiffness for the cases from bistable to pentastable.

5. Conclusion

In this study, we discovered a novel methodology for the design of a highly programmable multistable unit cell by harnessing a Kresling origami-inspired module with tensile string elements. More specifically, we proposed a Kresling origami-inspired unit composed of rigid bars that are allowed to freely rotate at its joints. From this assumption we showed that there is a rich deformation behavior between the nodes of the unit cell as the structure is deployed. These rich deformation behaviors inspired us to strategically connect tensile elements between the nodes to increase the multistability of the unit cell, where a stable configuration could be achieved in a region where we had two distinct strings whose changes in length were opposite.

To demonstrate the programmable multistability of the unit cell, we presented a case study for an eight-sided unit cell composed of bars with creases at its ends and strategically integrated tensile elements, where its potential energy equals to the sum of the energy from the stretching of the strings and the folding of the creases. Using this model, the design variables of the unit cell were the unstretched length value of the strings, the stress-free state of the creases, and the ratio between the torsional elastic constant of the creases and the tensile force of the strings. In this study, we showed that for the classic folding of Kresling we can achieve up to five stable configurations in a single unit cell. More specifically, it was found that as the ratio between the torsional elastic constant of the creases and the tensile force of the strings decreased, the number of distinct combinations of the design variables that will yield tristable, quadstable and pentastable unit cells significantly increased. Furthermore, we demonstrated the high and efficient programmability of the number of stable states per unit cell by simply changing the unstretched length value of one string. By increasing the unstretched length of this string we transformed the system from tristable to quadstable to pentastable. Additionally, by going beyond the classic folding of Kresling, we showed that the same behavior that was achieved for positive values of rotational angle could also be achieved for negative values with distinct strings. Hence, for the entire folding range of our proposed Kresling origami-inspired unit cell, we uncovered a total of ten stable configurations. Moreover, we designed and tested an experimental prototype that verified the analytical results.

Lastly, a case study was conducted to assess the effect of increasing the number of stable configurations per unit cell in a modular structure for mechanical property tuning. For the case of two unit cells in series, we demonstrated that the unit cell with more stable configurations can be much more programmable than the one with a lower number of stable states. More specifically, we showed that we would need a total of fifty-four bistable unit cells in series to match the programmable capabilities of two decastable ones. Hence, by increasing the number of stable configurations per unit cell we can significantly increase the programmable capabilities of the system while maintaining its size and weight at a minimum.

CRedit authorship contribution statement

Richard Rodriguez-Feliciano: Conceptualization, Methodology, Software, Validation, Formal analysis, Investigation, Data Curation, Writing - Original Draft, Visualization. **Kon-Well Wang (aka K. W. Wang):** Conceptualization, Methodology, Validation, Resources, Writing - Review & Editing, Supervision, Project administration, Funding acquisition.

Declaration of competing interest

The authors declare that they have no known competing financial interests or personal relationships that could have appeared to influence the work reported in this paper.

Data availability

The data will be made available upon request.

Acknowledgements

This research is supported by the University of Michigan Collegiate Professorship, the University of Michigan Rackham Merit Fellowship, the National Science Foundation Graduate Research Fellowship under Grant No. DGE 1841052, and the National Science Foundation under Award Number 2314560. Any opinion, findings, and conclusions or recommendations expressed in this material are those of the authors and do not necessarily reflect the views of the National Science Foundation.

References:

[1] Li S, Fang H, Sadeghi S, Bhovad P, Wang KW. Architected Origami Materials: How Folding Creates Sophisticated Mechanical Properties. Adv Mater 2019;31:1805282. https://doi.org/10.1002/adma.201805282.

[2] Meloni M, Cai J, Zhang Q, Sang-Hoon Lee D, Li M, Ma R, Parashkevov TE, Feng J. Engineering Origami: A Comprehensive Review of Recent Applications, Design Methods, and Tools. Adv Sci 2021;8:2000636. https://doi.org/10.1002/advs.202000636.

[3] Zhai Z, Wu L, Jiang H. Mechanical metamaterials based on origami and kirigami. Appl Phys Rev 2021;8:041319. https://doi.org/10.1063/5.0051088.

[4] Zhu Y, Schenk M, Filipov ET. A Review on Origami Simulations: From Kinematics, To Mechanics, Toward Multiphysics. Appl Mech Rev 2022;74. https://doi.org/10.1115/1.4055031.

[5] Fonseca LM, Rodrigues G V., Savi MA. An overview of the mechanical description of origami-inspired systems and structures. Int J Mech Sci 2022;223:107316. https://doi.org/10.1016/J.IJMECSCI.2022.107316.

[6] Misseroni D, Pratapa PP, Liu K, Kresling B, Chen Y, Daraio C, Paulino GH. Origami engineering. Nat Rev Methods Prim 2024;4:40. https://doi.org/10.1038/s43586-024-00313-7.

[7] Lu L, Leanza S, Zhao RR. Origami With Rotational Symmetry: A Review on Their Mechanics and Design. Appl Mech Rev 2023;75. https://doi.org/10.1115/1.4056637.

[8] Tachi T. Generalization of rigid-foldable quadrilateral-mesh origami. J Int Assoc Shell Spat Struct 2009;50:173–9.

[9] He Z, Guest SD. On rigid origami II: quadrilateral creased papers. Proc R Soc A Math Phys Eng Sci 2020;476:20200020. https://doi.org/10.1098/rspa.2020.0020.

[10] Schenk M, Guest SD. Geometry of Miura-folded metamaterials. Proc Natl Acad Sci 2013;110:3276–81. https://doi.org/10.1073/pnas.1217998110.

[11] Liu S, Lu G, Chen Y, Leong YW. Deformation of the Miura-ori patterned sheet. Int J Mech Sci 2015;99:130–42. https://doi.org/10.1016/j.ijmecsci.2015.05.009.

[12] Thota M, Wang KW. Reconfigurable origami sonic barriers with tunable bandgaps for traffic noise mitigation. J Appl Phys 2017;122:154901. https://doi.org/10.1063/1.4991026.

[13] Thota M, Li S, Wang KW. Lattice reconfiguration and phononic band-gap adaptation via origami folding. Phys Rev B 2017;95:64307. https://doi.org/10.1103/PhysRevB.95.064307.

[14] Silverberg JL, Evans AA, McLeod L, Hayward RC, Hull T, Santangelo CD, Cohen I. Using origami design principles to fold reprogrammable mechanical metamaterials. Science 2014;345:647–50. https://doi.org/10.1126/science.1252876.

[15] Lv Y, Zhang Y, Gong N, Li Z, Lu G, Xiang X. On the out-of-plane compression of a Miura-ori patterned sheet. Int J Mech Sci 2019;161–162:105022. https://doi.org/10.1016/j.ijmecsci.2019.105022.

[16] Fang H, Li S, Thota M, Wang KW. Origami lattices and folding-induced lattice transformations. Phys Rev Res 2019;1:23010. https://doi.org/10.1103/PhysRevResearch.1.023010.

[17] Hathcock M, Popa BI, Wang KW. Origami inspired phononic structure with metamaterial inclusions for tunable angular wave steering. J Appl Phys 2021;129:145103. https://doi.org/10.1063/5.0041503.

[18] Xia Y, Kidambi N, Filipov E, Wang KW. Deployment Dynamics of Miura Origami Sheets. J Comput Nonlinear Dyn 2022;17. https://doi.org/10.1115/1.4054109.

[19] Liu K, Pratapa PP, Misseroni D, Tachi T, Paulino GH. Triclinic Metamaterials by Tristable

Origami with Reprogrammable Frustration. Adv Mater 2022;34:2107998. https://doi.org/10.1002/adma.202107998.

[20] Tachi T, Miura K. Rigid-foldable cylinders and cells. J Int Assoc Shell Spat Struct 2012;53:217–26.

[21] Gattas JM, You Z. Geometric assembly of rigid-foldable morphing sandwich structures. Eng Struct 2015;94:149–59. https://doi.org/10.1016/j.engstruct.2015.03.019.

[22] Li S, Wang KW. Fluidic origami with embedded pressure dependent multi-stability: A plant inspired innovation. J R Soc Interface 2015;12. https://doi.org/10.1098/rsif.2015.0639.

[23] Fang H, Wang KW, Li S. Asymmetric energy barrier and mechanical diode effect from folding multi-stable stacked-origami. Extrem Mech Lett 2017;17:7–15. https://doi.org/10.1016/j.eml.2017.09.008.

[24] Fang H, Li S, Ji H, Wang KW. Dynamics of a bistable Miura-origami structure. Phys Rev E 2017;95:52211. https://doi.org/10.1103/PhysRevE.95.052211.

[25] Sengupta S, Li S. Harnessing the anisotropic multistability of stacked-origami mechanical metamaterials for effective modulus programming. J Intell Mater Syst Struct 2018;29:2933–45. https://doi.org/10.1177/1045389X18781040.

[26] Sadeghi S, Li S. Fluidic origami cellular structure with asymmetric quasi-zero stiffness for low-frequency vibration isolation. Smart Mater Struct 2019;28:065006. https://doi.org/10.1088/1361-665X/ab143c.

[27] Liu Z, Fang H, Xu J, Wang KW. A novel origami mechanical metamaterial based on Miura-variant designs: exceptional multistability and shape reconfigurability. Smart Mater Struct 2021;30:085029. https://doi.org/10.1088/1361-665X/ac0d0f.

[28] Liu Z, Fang H, Xu J, Wang KW. Discriminative Transition Sequences of Origami Metamaterials for Mechanologic. Adv Intell Syst 2023;5:2200146. https://doi.org/10.1002/aisy.202200146.

[29] Kresling B. Origami-structures in nature: lessons in designing “smart” materials. MRS Online Proc Libr 2012;1420:42–54. https://doi.org/10.1557/opl.2012.536.

[30] Masana R, Dalaq AS, Khazaaleh S, Daqaq MF. The Kresling origami spring: a review and assessment. Smart Mater Struct 2024;33:043002. https://doi.org/10.1088/1361-665X/ad2f6f.

[31] Wang X, Qu H, Zhao K, Yang X, Guo S. Kresling origami derived structures and inspired mechanical metamaterial. Smart Mater Struct 2024;33:075030. https://doi.org/10.1088/1361-665X/ad5a5a.

[32] Zang S, Misseroni D, Zhao T, Paulino GH. Kresling origami mechanics explained: Experiments and theory. J Mech Phys Solids 2024;188:105630. https://doi.org/10.1016/j.jmps.2024.105630.

[33] Kidambi N, Wang KW. Dynamics of Kresling origami deployment. Phys Rev E 2020;101:63003. https://doi.org/10.1103/PhysRevE.101.063003.

[34] Agarwal V, Wang KW. On the nonlinear dynamics of a Kresling-pattern origami under harmonic force excitation. Extrem Mech Lett 2022;52:101653. https://doi.org/10.1016/j.eml.2022.101653.

[35] Moshtaghzadeh M, Bakhtiari A, Izadpanahi E, Mardanpour P. Artificial Neural Network for the prediction of fatigue life of a flexible foldable origami antenna with Kresling pattern. Thin-Walled Struct 2022;174:109160. https://doi.org/10.1016/j.tws.2022.109160.

[36] Ye S, Zhao P, Zhao Y, Kavousi F, Feng H, Hao G. A Novel Radially Closable Tubular Origami Structure (RC-ori) for Valves. Actuators 2022;11. https://doi.org/10.3390/act11090243.

[37] Lu L, Dang X, Feng F, Lv P, Duan H. Conical Kresling origami and its applications to curvature and energy programming. Proc R Soc A Math Phys Eng Sci 2022;478:20210712. https://doi.org/10.1098/rspa.2021.0712.

[38] Yin P, Han H, Tang L, Tan X, Guo M, Xia C, Aw KC. Kresling origami-inspired electromagnetic energy harvester with reversible nonlinearity. Smart Mater Struct 2024;33:035043. https://doi.org/10.1088/1361-665X/ad27fb.

[39] Chung J, Song M, Chung SH, Choi W, Lee S, Lin ZH, Hong J, Lee S. Triangulated Cylinder Origami-Based Piezoelectric/Triboelectric Hybrid Generator to Harvest Coupled Axial and Rotational Motion. Research 2024;2021. https://doi.org/10.34133/2021/7248579.

[40] Yu X, Wang L. Nonlinear dynamics of coupled waves in Kresling origami metamaterials. J Sound Vib 2024;577:118263. https://doi.org/10.1016/j.jsv.2024.118263.

[41] Bhovad P, Kaufmann J, Li S. Peristaltic locomotion without digital controllers: Exploiting multi-stability in origami to coordinate robotic motion. Extrem Mech Lett 2019;32:100552. https://doi.org/10.1016/J.EML.2019.100552.

[42] Li Z, Kidambi N, Wang L, Wang KW. Uncovering rotational multifunctionalities of coupled Kresling modular structures. Extrem Mech Lett 2020;39:100795. https://doi.org/10.1016/J.EML.2020.100795.

[43] Huang C, Tan T, Wang Z, Nie X, Zhang S, Yang F, Lin Z, Wang, B, Yan Z. Bistable programmable origami based soft electricity generator with inter-well modulation. Nano Energy 2022;103:107775. https://doi.org/10.1016/j.nanoen.2022.107775.

[44] Zhang J, Zhang L, Wang C. Kresling origami-inspired reconfigurable antenna with spherical cap. Int J Mech Sci 2022;227:107470. https://doi.org/10.1016/j.ijmecsci.2022.107470.

[45] Bentley CS, Harne RL. Deployable linear and spiral array structures based on a Kresling-inspired mechanism with integrated scissor arms. J Intell Mater Syst Struct 2023;34:1917–31. https://doi.org/10.1177/1045389X231157355.

[46] Hu J, Pan H. Design of constant-force mechanisms using origami. Adv Mech Eng 2024;16. https://doi.org/10.1177/16878132241241475.

[47] Wilson L, Pellegrino S, Danner R. Origami Sunshield Concepts for Space Telescopes. 54th AIAA/ASME/ASCE/AHS/ASC Struct. Struct. Dyn. Mater. Conf., American Institute of Aeronautics and Astronautics; 2013. https://doi.org/doi:10.2514/6.2013-1594.

[48] Jianguo C, Xiaowei D, Ya Z, Jian F, Yongming T. Bistable Behavior of the Cylindrical Origami Structure With Kresling Pattern. J Mech Des 2015;137. https://doi.org/10.1115/1.4030158.

[49] Zhai Z, Wang Y, Jiang H. Origami-inspired, on-demand deployable and collapsible mechanical metamaterials with tunable stiffness. Proc Natl Acad Sci 2018;115:2032–7. https://doi.org/10.1073/pnas.1720171115.

[50] Pagano A, Yan T, Chien B, Wissa A, Tawfick S. A crawling robot driven by multi-stable origami. Smart Mater Struct 2017;26:094007. https://doi.org/10.1088/1361-665X/aa721e.

[51] Kaufmann J, Bhovad P, Li S. Harnessing the Multistability of Kresling Origami for Reconfigurable Articulation in Soft Robotic Arms. Soft Robot 2022;9:212–23.

https://doi.org/10.1089/soro.2020.0075.

[52] Reid A, Lechenault F, Rica S, Adda-Bedia M. Geometry and design of origami bellows with tunable response. Phys Rev E 2017;95:13002. https://doi.org/10.1103/PhysRevE.95.013002.

[53] Masana R, Daqaq MF. Quasi-static behavior of a pair of serially-connected Kresling Origami springs. Int J Solids Struct 2024;298:112877. https://doi.org/10.1016/j.ijsolstr.2024.112877.

[54] Li Z, Agarwal V, Wang L, Wang KW. On-demand tuning of mechanical stiffness and stability of Kresling origami harnessing its nonrigid folding characteristics. Smart Mater Struct 2023;32:085025. https://doi.org/10.1088/1361-665X/ace0eb.

[55] Wang X, Qu H, Li X, Kuang Y, Wang H, Guo S. Multi-triangles cylindrical origami and inspired metamaterials with tunable stiffness and stretchable robotic arm. PNAS Nexus 2023;2:pgad098. https://doi.org/10.1093/pnasnexus/pgad098.

[56] Liu Q, Ye H, Cheng J, Li H, He X, Jian B, Ge Q. Stiffness-Tunable Origami Structures via Multimaterial Three-Dimensional Printing. Acta Mech Solida Sin 2023;36:582–93. https://doi.org/10.1007/s10338-023-00403-1.

[57] Wu S, Ze Q, Dai J, Udipi N, Paulino GH, Zhao R. Stretchable origami robotic arm with omnidirectional bending and twisting. Proc Natl Acad Sci 2021;118:e2110023118. https://doi.org/10.1073/pnas.2110023118.

[58] Melancon D, Forte AE, Kamp LM, Gorissen B, Bertoldi K. Inflatable Origami: Multimodal Deformation via Multistability. Adv Funct Mater 2022;32:2201891. https://doi.org/10.1002/adfm.202201891.

[59] Jianguo C, Xiaowei D, Yuting Z, Jian F, Ya Z. Folding Behavior of a Foldable Prismatic Mast With Kresling Origami Pattern. J Mech Robot 2016;8. https://doi.org/10.1115/1.4032098.

[60] Zhang C, Zhang Z, Peng Y, Zhang Y, An S, Wang Y, Zhai Z, Xu Y, Jiang H. Plug & play origami modules with all-purpose deformation modes. Nat Commun 2023;14:4329. https://doi.org/10.1038/s41467-023-39980-7.

[61] Wang Y, Zhang X, Zhu S. Highly intensive and controllable supratransmission in a Kresling-origami metastructure. Extrem Mech Lett 2023;59:101964. https://doi.org/10.1016/J.EML.2023.101964.

[62] Xu Z-L, Wang Y-Q, Zhu R, Chuang K-C. Torsional bandgap switching in metamaterials with compression–torsion interacted origami resonators. J Appl Phys 2021;130:045105. https://doi.org/10.1063/5.0056179.

[63] Han H, Sorokin V, Tang L, Cao D. Origami-based tunable mechanical memory metamaterial for vibration attenuation. Mech Syst Signal Process 2023;188:110033. https://doi.org/10.1016/j.ymssp.2022.110033.

[64] Miyazawa Y, Chen C-W, Chaunsali R, Gormley TS, Yin G, Theocharis G, et al. Topological state transfer in Kresling origami. Commun Mater 2022;3:62. https://doi.org/10.1038/s43246-022-00280-0.

[65] Novelino LS, Ze Q, Wu S, Paulino GH, Zhao R. Untethered control of functional origami microrobots with distributed actuation. Proc Natl Acad Sci 2020;117:24096–101. https://doi.org/10.1073/pnas.2013292117.

[66] Masana R, Khazaaleh S, Alhussein H, Crespo RS, Daqaq MF. An origami-inspired dynamically

actuated binary switch. Appl Phys Lett 2020;117:081901. https://doi.org/10.1063/5.0010236.

[67] Yasuda H, Tachi T, Lee M, Yang J. Origami-based tunable truss structures for non-volatile mechanical memory operation. Nat Commun 2017;8. https://doi.org/10.1038/s41467-017-00670-w.

[68] Jules T, Reid A, Daniels KE, Mungan M, Lechenault F. Delicate memory structure of origami switches. Phys Rev Res 2022;4:13128. https://doi.org/10.1103/PhysRevResearch.4.013128.

[69] Wo Z, Filipov ET. Stiffening multi-stable origami tubes by outward popping of creases. Extrem Mech Lett 2023;58:101941. https://doi.org/10.1016/J.EML.2022.101941.

[70] Wang X, Qu H, Guo S. Tristable property and the high stiffness analysis of Kresling pattern origami. Int J Mech Sci 2023;256:108515. https://doi.org/10.1016/J.IJMECSCI.2023.108515.

[71] Yang X, Keten S. Multi-Stability Property of Magneto-Kresling Truss Structures. J Appl Mech 2021;88:91009. https://doi.org/10.1115/1.4051705.

[72] Huang C, Tan T, Hu X, Yang F, Yan Z. Bio-inspired programmable multi-stable origami. Appl Phys Lett 2022;121:051902. https://doi.org/10.1063/5.0088242.

[73] Zhang Z, Chen G, Wu H, Kong L, Wang H. A Pneumatic/Cable-Driven Hybrid Linear Actuator With Combined Structure of Origami Chambers and Deployable Mechanism. IEEE Robot Autom Lett 2020;5:3564–71. https://doi.org/10.1109/LRA.2020.2976324.

[74] Ochalek M, Arya M. Design and Modeling of Pre-stressed, Flat-Folding, Modular Origami Tube Structures. AIAA SCITECH 2024 Forum, American Institute of Aeronautics and Astronautics; 2024. https://doi.org/doi:10.2514/6.2024-1043.

[75] Jeong D, Lee K. Design and analysis of an origami-based three-finger manipulator. Robotica 2018;36:261–74. https://doi.org/DOI: 10.1017/S0263574717000340.

[76] Lee K, Wang Y, Zheng C. TWISTER Hand: Underactuated Robotic Gripper Inspired by Origami Twisted Tower. IEEE Trans Robot 2020;36:488–500. https://doi.org/10.1109/TRO.2019.2956870.

[77] Santoso J, Skorina EH, Luo M, Yan R, Onal CD. Design and analysis of an origami continuum manipulation module with torsional strength. 2017 IEEE/RSJ Int. Conf. Intell. Robot. Syst., 2017, p. 2098–104. https://doi.org/10.1109/IROS.2017.8206027.

[78] Ma S, Chen M, Zhang H, Skelton RE. Statics of integrated origami and tensegrity systems. Int J Solids Struct 2023;279:112361. https://doi.org/10.1016/j.ijsolstr.2023.112361.

[79] Liu K, Kosednar M, Tachi T, Paulino GH. Integrated Origami-String System. Int. Des. Eng. Tech. Conf. Comput. Inf. Eng. Conf., vol. 59247, American Society of Mechanical Engineers; 2019, p. V05BT07A033.

[80] Silverberg JL, Na J-H, Evans AA, Liu B, Hull TC, Santangelo CD, Lang RJ, Hayward RC, Cohen I. Origami structures with a critical transition to bistability arising from hidden degrees of freedom. Nat Mater 2015;14:389–93. https://doi.org/10.1038/nmat4232.

[81] Simaite A, Temple B, Karimi MA, Alizadehyazdi V, Spenko M. Understanding the influence of silicone elastomer properties on wedge-shaped microstructured dry adhesives loaded in shear. J R Soc Interface 2018;15. https://doi.org/10.1098/rsif.2018.0551.